

Evaluation of Virtual Synchronous Machines with Dynamic or Quasi-Stationary Machine Models

Olve Mo, Salvatore D'Arco and Jon Are Suul, *Member, IEEE*

Abstract—This paper presents a comparison of the small-signal stability properties for Virtual Synchronous Machines (VSMs) with dynamic and quasi-stationary representation of the internal Synchronous Machine (SM) model. It is shown that the dynamic electrical equations may introduce poorly damped oscillations when realistic stator impedance values for high power SMs are used. The quasi-stationary implementation is less sensitive to the impedance of the virtual machine model, but depends on filtering of the measured d- and q- axis components of the ac-side voltage to avoid instability or poorly damped oscillations. It is demonstrated how both implementations can be made stable and robust for a wide range of grid impedances. However, the dynamic electrical model depends on a high virtual resistance for effectively damping internal oscillations associated with dc-components in the ac currents during transients. Thus, when using SM parameters with low virtual stator resistance for decoupling the active and reactive power control, the quasi-stationary VSM implementation is preferable.

Index Terms— Small-Signal Stability, Synchronous Machine Swing Equation, Virtual Synchronous Machine

I. INTRODUCTION

CONTROL strategies based on the concept of Virtual Synchronous Machines (VSMs) have the potential to become a flexible framework for providing converter-based grid services in future power systems. Indeed, VSM based control strategies for Voltage Source Converters (VSCs) have especially been developed to serve two main purposes [1]-[5]:

- i) Providing virtual inertia and thereby contributing to the total equivalent inertia of the grid.

Manuscript received, April 30, 2016, revised September 10, 2016, accepted September 24, 2016. The work of SINTEF Energy Research in this paper was supported by the project "Releasing the Potential of Virtual Synchronous Machines – ReViSM" through the Blue Sky instrument of SINTEF Energy Research as a Strategic Institute Programme (SIP) financed by the national Basic Funding Scheme of Norway

O. Mo and S. D'Arco are with SINTEF Energy Research, 7465 Trondheim, Norway, (e-mail: Olve.Mo@sintef.no, Salvatore.D'Arco@sintef.no)

J. A. Suul is with SINTEF Energy Research, 7465 Trondheim, Norway, and with the Department of Electric Power Engineering, Norwegian University of Science and Technology, 7495 Trondheim, Norway, e-mail: Jon.A.Suul@sintef.no

- ii) Enabling operation in both grid-connected and islanded system configurations without any change of control structure and parameters.

To obtain both these functionalities, VSMs must rely on a similar power-balance-based synchronization mechanism as Synchronous Machines (SMs). Thus, VSMs will not depend on conventional Phase Locked Loops (PLLs) for grid synchronization [5], [6].

All VSM implementations include a representation of a SM, executed in real time to generate internal control references. The internal model can represent the SM behavior with different degrees of fidelity, while it must be formulated according to the interfaces with the other control loops of the power converter. In general, there are two dominating architectures, depending on whether the machine model provides a current reference or a voltage reference for controlling the converter operation [6]. Examples of VSM implementations where the internal SM model generates references for a current controller have for instance been presented in [1] [4], [5], [7]-[11]. Alternatively, the internal SM model can provide voltage references, as discussed for different implementations of the voltage control in [12]-[16], [17] and [18]-[21], respectively.

Among the current-based VSM implementations, the electrical part of the internal SM model can be represented with two different approaches. Indeed, the first proposals of VSM-based control included modelling of the dynamic electrical equations of the SM [1], [3]-[5], [7]-[14]. However, implementations based on a quasi-stationary representation of the SM stator windings have recently been proposed in [22], [23]. The quasi-stationary approach introduces a further simplification of the modelling, since all transient electrical dynamics of the emulated SM are neglected. Both these two types of implementations have been individually demonstrated by numerical simulations and/or laboratory experiments. In general, it is also clear that the steady-state behavior will be identical for these two types of implementations while differences will appear in the transient performances. However, from previous publications it is not clear which implementation will have the most preferable dynamic properties.

This paper is presenting a comparison and assessment of dynamic properties and small-signal stability of VSM implementations based on a Dynamic Electrical Model (DEM) or a Quasi-Stationary Electrical Model (QSEM). For this purpose, implementations of DEM- and QSEM-based VSMs

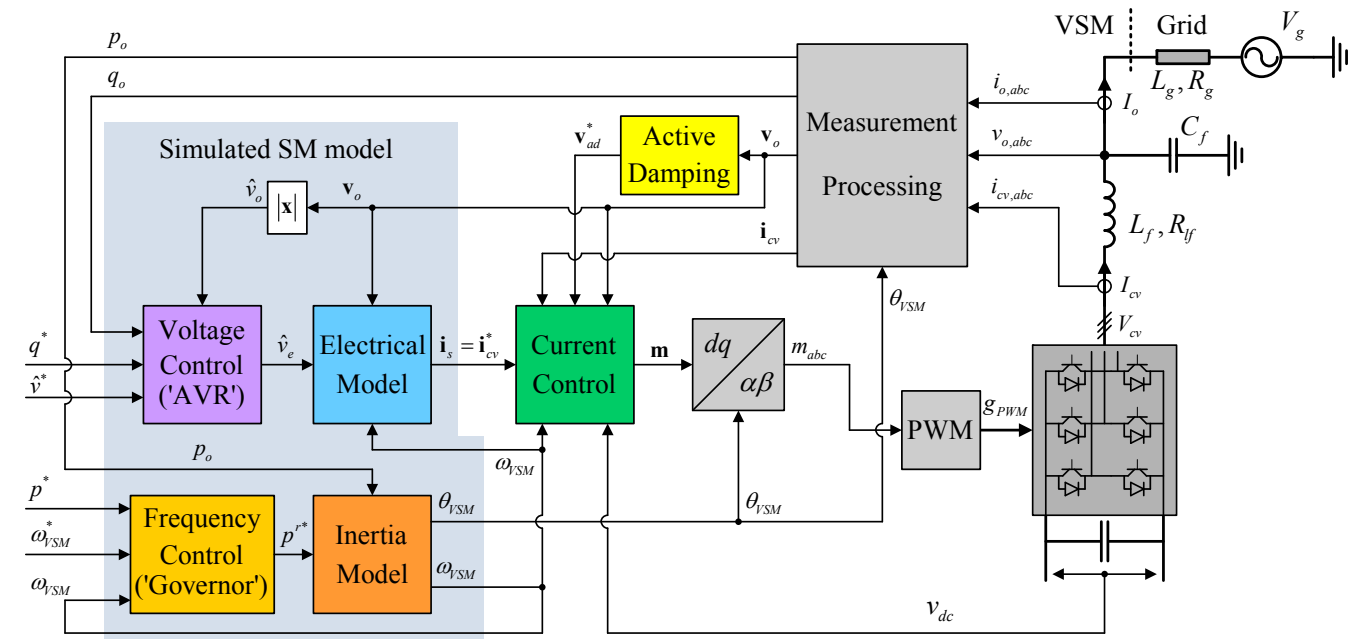


Fig. 1 Overview of the investigated VSM implementations

are adapted from [4], [5], [7], [8] and [22], [23] respectively, into a common framework for comparison. Linearized small-signal state-space models of both alternatives are also developed, and their validity is verified by time-domain simulations. These small-signal models are used to analyze the sources of critical oscillation modes and to ensure stability in a wide range of operating conditions.

From the developed models, it is demonstrated how the implementation with dynamic electrical equations requires relatively high values of the stator resistance to avoid poorly damped oscillations. Such a high stator resistance implies that there will be a stronger coupling between the active and reactive power flow through the emulated stator impedance, causing a nonlinear coupling between the corresponding active and reactive power control loops. On the other hand, the QSEM implementation depends on low-pass filtering of the d- and q-axis voltages measured at the ac-side to ensure stability when the VSC is interfaced to the grid with a LC- or LCL filter. However, the QSEM-based implementation can offer satisfactory performances also with a purely inductive electrical SM stator model. Thus, the QSEM implementation is shown to be preferable for obtaining decoupling between active and reactive power control.

II. SYNCHRONOUS MACHINE ELECTRICAL MODELS FOR CURRENT REFERENCES GENERATION

A general overview of the VSM-based control systems and the power system configuration considered in this paper is shown in Fig. 1. A model of an SM and its associated control loops is providing current references for the inner loop control of a three-phase VSCs. The blocks composing the internal representation of the SM and its traditional control loops are grouped in the left of the figure. This internal model contains a representation of a simplified swing equation as the inertia model, and a frequency controller emulating the simplified behavior of a prime mover with its speed governor. Moreover,

an electrical model and a voltage controller are representing the stator windings of an SM and the associated Automatic Voltage Regulator (AVR). For presenting a fair comparison, the only difference between the DEM-based and the QSEM-based VSM implementations investigated in this paper is the representation of the SM stator windings within the block "Electrical Model" in Fig. 1, as will be explained in the following.

A. Modeling conventions

In this paper, physical values are denoted with upper case symbols, while the control system and the mathematical modeling is presented in per unit quantities denoted with lower case symbols. The base values of the per unit system are defined from the apparent power rating of the VSM and the rated peak value of the phase voltage [24]. Moreover, electrical models will be expressed in a Synchronously Rotating Reference Frame (SRRF) by an amplitude invariant Park transformation. Whenever possible, SRRF equations are presented in complex space-vector notation according to:

$$\mathbf{x} = x_d + j \cdot x_q \quad (1)$$

B. Dynamic electrical SM model

In case of a DEM-based VSM implementation, the block labelled "Electrical model" in Fig.1 consists of a controlled voltage source \mathbf{v}_e representing the internally induced voltage of a SM, in series with a dynamic representation of an RL impedance representing the virtual stator windings. The LC-filter output voltage \mathbf{v}_o is measured and used as an input to the internally simulated electric model. Then, the virtual stator currents, \mathbf{i}_s^{DEM} , calculated by the numerical simulation of the model, are provided as references to the VSC current controllers [4], [5]. The transient and sub-transient behaviors of an SM are intentionally not modelled.

Using complex space-vector notation, the DEM model can be expressed in a SRRF by (2).

$$\frac{d\mathbf{i}_s^{DEM}}{dt} = \frac{\omega_b}{l_s} \mathbf{v}_e - \frac{\omega_b}{l_s} \mathbf{v}_o - \left(\frac{r_s \omega_b}{l_s} + j \cdot \omega_{VSM} \omega_b \right) \mathbf{i}_s \quad (2)$$

In this equation, r_s and l_s are the virtual stator resistance and inductance, while ω_b is the base angular frequency, and ω_{VSM} is the per unit speed of the virtual inertia. The d-axis of the SRRF used for the modelling is aligned with the internal voltage vector \mathbf{v}_e of the VSM (i.e. $\mathbf{v}_e = \hat{v}_e$).

C. Quasi-stationary electrical SM model

The Quasi-Stationary Electrical Model (QSEM) implementation assumes an algebraic (i.e. phasor-based) representation of the SM stator impedance in the SRRF. This is equivalent to setting the current derivative in (2) to zero, resulting in the quasi-stationary stator current [22], [23]:

$$\mathbf{i}_s^{QS} = \frac{\mathbf{v}_e - \mathbf{v}_o}{(r_s + j \cdot \omega_{VSM} l_s)} \quad (3)$$

However, it will be shown later that it is necessary to include a low pass filter in the measurement of \mathbf{v}_o to prevent oscillatory or even unstable operation of the QSEM-based VSM. Thus, the measured filter capacitor voltage \mathbf{v}_o in (3) should be replaced by the outputs \mathbf{v}_m from low-pass filters on the d - and q -axis voltages in the SRRF, as defined by

$$\frac{d\mathbf{v}_m}{dt} = \omega_{vf} \cdot \mathbf{v}_o - \omega_{vf} \cdot \mathbf{v}_m \quad (4)$$

where ω_{vf} is the crossover frequency of the low-pass filter. Replacing \mathbf{v}_o by \mathbf{v}_m and expanding the expression in (3), the virtual SM stator currents, \mathbf{i}_s^{QSEM} , that should be used as references for the VSC current control in the case of the QSEM can be expressed as:

$$\mathbf{i}_s^{QSEM} = \frac{\mathbf{v}_e - \mathbf{v}_m}{(r_s + j \cdot \omega_{VSM} l_s)} = \frac{r_s (\mathbf{v}_e - \mathbf{v}_m)}{r_s^2 + (\omega_{VSM} l_s)^2} - j \frac{\omega_{VSM} l_s (\mathbf{v}_e - \mathbf{v}_m)}{r_s^2 + (\omega_{VSM} l_s)^2} \quad (5)$$

It can be noted that due to the low-pass filter, both the QSEM and the DEM implementations result in two first order differential equations for the internal SM representation in the SRRF. It is also clear from the presented equations that the two models become identical in steady state.

III. MATHEMATICAL MODELLING OF INVESTIGATED VSM IMPLEMENTATIONS

In order to compare the performance and dynamic properties of the two investigated groups of VSM implementations, a model of the system shown in Fig. 1 is established on state-space form, including the SM emulation, the corresponding outer control loops, the VSC current controllers and the electrical circuit. It should be noted that the implementations of DEM- and QSEM-based VSMS presented in the literature are developed and presented in different contexts. Thus, the overall control systems presented in the literature are not directly comparable. For instance the reference frame used for the VSM implementation, the applied current control loops and also the implementation of the virtual swing equations differ between the control systems in [4], [5], [7], [8] and [22], [23], respectively. To ensure a fair comparison that can reveal the main implications of using DEM- and QSEM-based approaches for providing current references, the VSM implementations from the literature have

been adapted to a common implementation, as fully revealed in the following sub-sections. The mathematical models of all functional blocks are presented in order to establish first a non-linear state-space model and then a corresponding small-signal model for eigenvalue analysis.

A. Electrical system model and inner loop controllers

As shown in Fig. 1, the investigated configuration consists of a VSM-controlled VSC connected to an external grid through a LC filter, and the VSC is operated with conventional decoupled PI current controllers in the SSRF. Thus, the state-space equations of the electrical system, the current controllers and the active damping algorithm assumed for suppressing LC filter oscillations are well established and can be directly adapted from [19], [20], [25]. The equations for the currents in the filter inductor, the grid side currents, and the voltage of the filter capacitor can be derived directly from the circuit in Fig. 1, and are not presented for brevity. However, the voltage output from the current controller can be expressed by:

$$\mathbf{v}_{cv}^* = k_{pc} (\mathbf{i}_{cv}^* - \mathbf{i}_{cv}) + k_{ic} \cdot \boldsymbol{\gamma} + j \cdot l_f \cdot \omega_{vsm} \cdot \mathbf{i}_{cv} - \mathbf{v}_{ad}^* \quad (6)$$

$$\frac{d\boldsymbol{\gamma}}{dt} = \mathbf{i}_{cv}^* - \mathbf{i}_{cv}$$

where $\boldsymbol{\gamma}$ is representing the states of the integral term in the decoupled PI currents controllers implemented in the SSRF. As indicated in Fig. 1, the current reference \mathbf{i}_{cv}^* is equal to the current \mathbf{i}_s resulting from the simulated SM model, and will be given by \mathbf{i}_s^{DEM} or \mathbf{i}_s^{QSEM} depending on the studied VSM implementation.

In these equations, the switching effects are neglected and the VSC is represented by an ideal average model. Furthermore, it is assumed that the modulation index for the converter is calculated by dividing the voltage reference \mathbf{v}_{cv}^* from the current controllers by the measured dc voltage v_{dc} according to (7). Thus, the converter output voltage, \mathbf{v}_{cv} , will be decoupled from possible transients in the dc side. This implies that the converter output voltage will be equal to its reference value, and that representation of the dc-side will not be necessary for assessing dynamic properties on the ac-side.

$$\mathbf{m} = \frac{\mathbf{v}_{cv}^*}{v_{dc}}, \quad \mathbf{v}_{cv} = \mathbf{m} \cdot v_{dc} \quad \rightarrow \quad \mathbf{v}_{cv} = \mathbf{v}_{cv}^* \quad (7)$$

For suppressing oscillations in the LC-filter shown in Fig. 1, a simple strategy for active damping according to [26], [27] is included in the current controller output voltage according to (6). The damping voltage \mathbf{v}_{ad}^* , is given by (8), where the states $\boldsymbol{\phi}$ represent low-pass filters implemented in the SSRF.

$$\mathbf{v}_{ad}^* = k_{ad} (\mathbf{v}_o - \boldsymbol{\phi})$$

$$\frac{d\boldsymbol{\phi}}{dt} = \omega_{ad} \cdot \mathbf{v}_o - \omega_{ad} \cdot \boldsymbol{\phi} \quad (8)$$

B. Inertia model

The inertia model of a VSM can be conveniently represented by a linearized swing equation of a SM [6], [16], [28]. A real SM will exhibit a damping torque almost proportional to the difference between the grid frequency and the frequency given by the rotational speed of the machine. A similar torque or power can be easily included in the VSM

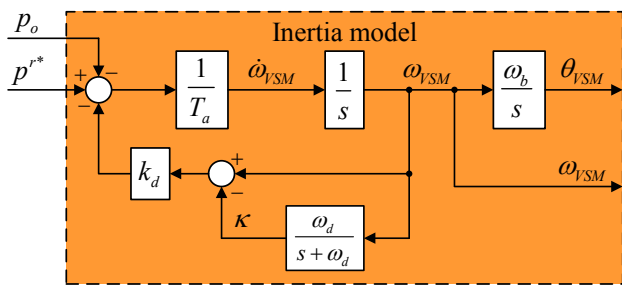


Fig. 2 VSM inertia model

inertia model if the grid frequency is available in the control (e.g. from a PLL) [16], [19]. However, for the implementation shown in Fig. 2, the damping is instead introduced by adding a high-pass filtered negative feedback from the VSM [29]. The high-pass filtering is implemented by using a low-pass filter with crossover frequency of ω_d and the high-pass filtered signal ($\omega_{VSM} - \kappa$) is multiplied with a gain of k_d . This damping will be almost equivalent to the damping in a real SM if the grid frequency changes relatively slowly compared to the dynamics of the emulated VSM speed.

The state equations for the inertia model from Fig. 2, corresponding to the block labeled "Inertia Model" in Fig. 1, are defined by:

$$\begin{aligned} \frac{d\omega_{VSM}}{dt} &= \frac{p^*}{T_a} - \frac{p_o}{T_a} - \frac{k_d \cdot (\omega_{VSM} - \kappa)}{T_a} \\ \frac{d\kappa}{dt} &= \omega_d \cdot \omega_{VSM} - \omega_d \cdot \kappa \\ \frac{d\theta_{VSM}}{dt} &= \omega_{VSM} \cdot \omega_b \end{aligned} \quad (9)$$

where p^* is the virtual power driving the inertia, p_o is the measured power delivered to the grid and T_a is the mechanical time constant (equivalent to $2H$ in traditional SM models) [28]. The state of the low-pass filter used for the implementation of the damping is defined by κ , while the angle θ_{VSM} is the angle between the VSM-oriented rotating frame of the model and the stationary frame. Thus, θ_{VSM} is the instantaneous angle used for SRRF transformations.

For state-space modelling and small-signal stability analysis, the system must be represented in an SRRF where all variables will reach constant values in steady-state operation. Therefore, the phase angle of the VSM inertia must be referred to the phase angle of the grid voltage vector in the SRRF. For this purpose, the state $\delta\theta_{VSM}$ is introduced as:

$$\delta\theta_{VSM} = \theta_{VSM} - \theta_g \quad (10)$$

where θ_g is the phase angle of the grid voltage relative to the stationary frame. Thus, the last equation in (9) can be represented in the SRRF as:

$$\frac{d\delta\theta_{VSM}}{dt} = \omega_{VSM} \cdot \omega_b - \omega_g \cdot \omega_b \quad (11)$$

C. Measurement processing and SRRF orientation

The block labelled "Measurement Processing" in Fig. 1, contains the SRRF transformations from the three-phase measurements in the ac circuit, as well as the calculation of feedback signals for the outer loops. The active and reactive powers flowing into the grid are calculated according to (12).

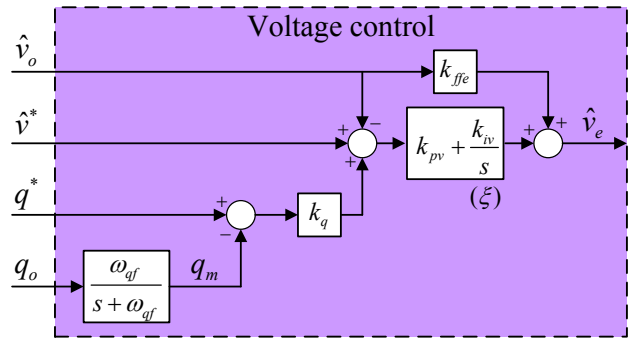


Fig. 3 Voltage Controller with reactive power droop ("AVR" in Fig. 1)

$$p_o = v_{o,d} \cdot i_{o,d} + v_{o,q} \cdot i_{o,q} \quad (12)$$

$$q_o = -v_{o,d} \cdot i_{o,q} + v_{o,q} \cdot i_{o,d}$$

As indicated in Fig. 1, the voltage amplitude \hat{v}_o can be calculated from the measured dq voltage components as:

$$\hat{v}_o = \sqrt{v_{o,d}^2 + v_{o,q}^2} \quad (13)$$

The SRRF applied for the control and modeling of the system is given by the angular position of the internally induced voltage, \mathbf{v}_e , as defined by the virtual inertia. Thus, modelling of the system depends on representation of the grid voltage vector in the SRRF defined by the VSM. With $\hat{\mathbf{v}}_g$ defining the grid voltage vector, the d - and q -axis components in the SRRF are defined by using (10) and (11):

$$\mathbf{v}_g = \hat{\mathbf{v}}_g e^{-j(\theta_{VSM} - \theta_g)} = \hat{\mathbf{v}}_g e^{-j\delta\theta_{VSM}} \quad (14)$$

D. VSM Outer Control Loops

The frequency control ('Governor'), indicated in Fig. 1 is modeled as an ideal power source able to provide instantly the power required. The power reference p^* for the ideal prime mover is generated by an outer frequency droop regulator according to:

$$p^* = p^* + k_\omega \cdot (\omega_{VSM}^* - \omega_{VSM}) \quad (15)$$

where p^* is the external power reference, ω_{VSM}^* is the VSM speed reference and k_ω is the frequency droop gain.

A voltage controller regulates the amplitude of the internally induced voltage \hat{v}_e of the VSM electric model, to control the voltage amplitude \hat{v}_o at the VSC filter capacitor. The control structure is shown in Fig. 3, which represents the block labelled Automatic Voltage Controller ('AVR') in Fig. 1. A standard PI-controller with gains k_{pv} and k_{iv} acts on the voltage amplitude error calculated as difference between the amplitude set-point \hat{v}^* and measured output voltage amplitude \hat{v}_o . The controller offers the possibility to activate a droop function in the voltage reference, based on the gain k_q and the difference between the low-pass filtered reactive power measurement q_m and the reactive power set-point q^* . In this case, q^* defines the level of reactive power at which the droop effect on the voltage set-point changes from a positive to a negative value. The equation for the output of the voltage controller is given by:

$$\hat{v}_e = k_{pv} \cdot (\hat{v}^* - \hat{v}_o) + k_{pv} \cdot k_q (q^* - q_m) + k_{iv} \cdot \xi + k_{ffe} \cdot \hat{v}_o \quad (16)$$

where the state equations for q_m and ξ , representing the low-pass filtered reactive power and the integrator state of the PI controller, respectively, are given by (17).

$$\begin{aligned} \frac{dq_m}{dt} &= \omega_{qf} \cdot q - \omega_{qf} \cdot q_m \\ \frac{d\xi}{dt} &= (\hat{v}^* - \hat{v}_o) + k_q (q^* - q_m) \end{aligned} \quad (17)$$

E. State-space representation and small-signal model

The models introduced in the previous subsections are combined together into a non-linear state-space model for both VSM implementations. The state vector \mathbf{x} of these models contain 17 state variables, as given by (18) for the DEM-based VSM implementation and by (19) for the QSEM-based VSM. The vector \mathbf{u} contains 7 input variables and is identical for the two models, as given by (20).

$$\mathbf{x}_{DEM} = \begin{bmatrix} v_{o,d} & v_{o,q} & i_{cv,d} & i_{cv,q} & \gamma_d & \gamma_q & i_{o,d} & i_{o,q} & \varphi_d \dots \\ \dots & \varphi_q & \xi & i_{s,d} & i_{s,q} & q_m & \omega_{VSM} & \delta\theta_{VSM} & \kappa \end{bmatrix} \quad (18)$$

$$\mathbf{x}_{QSEM} = \begin{bmatrix} v_{o,d} & v_{o,q} & i_{cv,d} & i_{cv,q} & \gamma_d & \gamma_q & i_{o,d} & i_{o,q} & \varphi_d \dots \\ \dots & \varphi_q & \xi & v_{m,d} & v_{m,q} & q_m & \omega_{VSM} & \delta\theta_{VSM} & \kappa \end{bmatrix} \quad (19)$$

$$\mathbf{u} = \begin{bmatrix} p^* & q^* & \hat{v}_{g,d} & \hat{v}_{g,q} & \hat{v}^* & \omega_{VSM}^* & \omega_g \end{bmatrix} \quad (20)$$

The detailed state-space equations of the two models are listed in the Appendix.

The steady-state operating conditions of the system can be calculated from the input signals by solving the set of state equations in the Appendix with the time derivatives set to zero. Thus, the model can be linearized around the resulting operating point \mathbf{x}_0 to obtain a small-signal state-space model of the system on the general form of (21) [24] :

$$\Delta \dot{\mathbf{x}} = \mathbf{A}(\mathbf{x}_0) \cdot \Delta \mathbf{x} + \mathbf{B}(\mathbf{x}_0) \cdot \Delta \mathbf{u} \quad (21)$$

IV. COMPARATIVE ANALYSIS FOR A REFERENCE CASE

As a first step, a comparative analysis between the two VSM implementations is conducted for a case with typical SM parameters and settings of the controllers based on tuning rules or performance criteria commonly applied to power converters [30], [31]. This reference case aims to provide an overview of the qualitative behavior of the two schemes and to identify the most critical parameters in a realistic operating scenario.

The test case is based on a low voltage application with a converter rated 2.75 MVA at 690 V. A 0.25 pu inductance, as a typical transient value for solid rotor generators [32], and a winding resistance equal to 0.01 pu are assumed for the virtual stator impedance. A list of the ratings and parameter values is reported in Table III in Appendix. The operating conditions defining the linearization point are corresponding to the set of references given in Table III.

A. Dynamic response and small-signal model validation

The results from simulation models in Matlab/Simulink ("Non-linear") are compared to the time domain response of the linearized small-signal models ("Linearized") for DEM and QSEM models in Fig. 4 a) and b), respectively, when applying the parameters in Table III. From these two figures, it is clearly seen that the small-signal models are accurately representing the dynamics of the nonlinear system models for small perturbations around the linearization point.

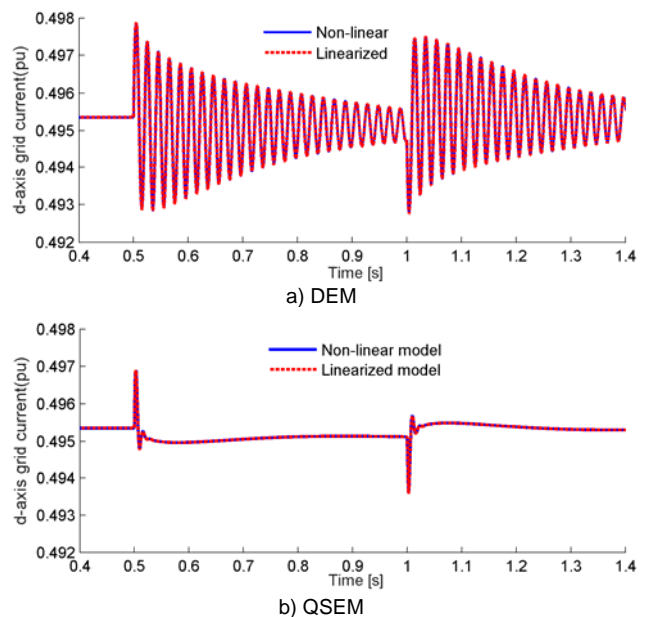


Fig. 4 Comparison between non-linear model and linearized state-space model - time domain simulation of transient after 0.001 pu step reduction in grid voltage amplitude between time 0.5 and 1.0 sec.

Furthermore, the curves in Fig. 4 show that the VSM implementation based on the DEM model results in poorly damped oscillations in the currents, which can also be shown to reflect in other system variables. The frequency of the observed oscillations is about 50 Hz in the SRRF, and these oscillations are indeed associated with a dc-current component in the stationary reference frame. Thus, the poorly damped response is reflecting the "synchronous frequency resonance" of the DEM-based VSM-implementation, equivalent to the discussion in [33]. Indeed, this effect corresponds to the dc components of the stator currents in an SM exposed to grid voltage perturbations. However, in a physical machine the dc component will be more effectively damped by the sub-transient impedance of the machine, while the current controllers of the studied VSM implementations will make the VSC to follow any dc component in the current reference resulting from the electrical model of the stator windings, without any additional damping. Thus, the DEM model will depend on much higher virtual stator resistance than the typical values for large SMs, or on other damping strategies as discussed in [33], to obtain an acceptable dynamic response.

As shown in Fig. 4 b), the QSEM-based VSM implementation do not suffer from the same poorly damped oscillations as the DEM-based implementation. Instead, this implementation shows only a small and fast transient followed by a slow settling to a new stationary operating condition according to the inertial dynamics. Thus, the QSEM-based VSM implementation is clearly favorable for operation with low values of the virtual stator resistance of the SM model

B. Eigenvalue analysis

To further analyze and compare the two VSM implementations, the eigenvalues of the corresponding small-signal models have been calculated for the operating conditions used in the previous section. A systematic parametric sensitivity analysis of the eigenvalues will be

TABLE I
SYSTEM EIGENVALUES

DEM Initial	DEM Final	QSEM Initial	QSEM Final
$\lambda_{1,2} = -1699 \pm 6510i$	$\lambda_{1,2} = -1697 \pm 6517i$	$\lambda_{1,2} = -2678 \pm 7869i$	$\lambda_{1,2} = -2558 \pm 7231i$
$\lambda_{3,4} = -1866 \pm 6152i$	$\lambda_{3,4} = -1864 \pm 6158i$	$\lambda_{3,4} = -398 \pm 4725i$	$\lambda_{3,4} = -1644 \pm 5778i$
$\lambda_{5,6} = -1428 \pm 260i$	$\lambda_{5,6} = -1490 \pm 260i$	$\lambda_{5,6} = -2917 \pm 2450i$	$\lambda_{5,6} = -697 \pm 248i$
$\lambda_{7,8} = -3.44 \pm 312i$	$\lambda_{7,8} = -61.0 \pm 305i$	$\lambda_{7,8} = -191 \pm 473i$	$\lambda_{7,8} = -284 \pm 262i$
$\lambda_9 = -193$	$\lambda_9 = -192$	$\lambda_9 = -192$	$\lambda_{9,10} = -55.2 \pm 14.4i$
$\lambda_{10,11} = -57.9 \pm 18.5i$	$\lambda_{10,11} = -56.9 \pm 17.7i$	$\lambda_{10,11} = -57.3 \pm 17.3i$	$\lambda_{12} = -38.7$
$\lambda_{12} = -39.3$	$\lambda_{12} = -38.0$	$\lambda_{12} = -39.0$	$\lambda_{13,14} = -5.67 \pm 8.62i$
$\lambda_{13,14} = -5.86 \pm 8.32i$	$\lambda_{13,14} = -6.23 \pm 9.04i$	$\lambda_{13,14} = -5.81 \pm 8.43i$	$\lambda_{15} = -8.72$
$\lambda_{15} = -9.02$	$\lambda_{15,16} = -9.35 \pm 0.27i$	$\lambda_{15} = -8.98$	$\lambda_{15} = -10.7$
$\lambda_{16} = -10.6$	$\lambda_{17} = -12.0$	$\lambda_{16} = -10.6$	$\lambda_{16} = -12.2$
$\lambda_{17} = -12.2$		$\lambda_{17} = -12.2$	$\lambda_{17} = -200$

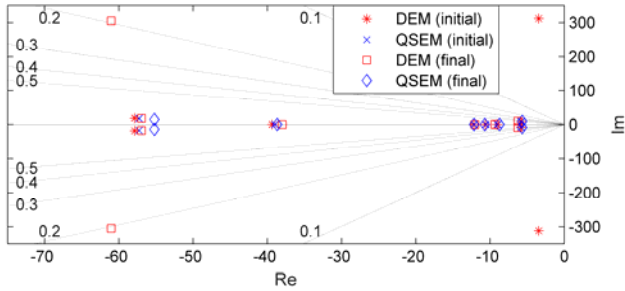


Fig. 5 Zoomed plot of eigenvalues for the two implementations with initial and final settings

presented in a separate section, but some results are anticipated in this section to refine the reference case settings and improve the performances to a reasonable level for further comparison. More specifically, the stator resistance r_s of the DEM-based implementation is increased to 0.1 pu. Similarly, the crossover frequency of the low-pass filtering of v_o used in the QSEM-based implementation have been changed from 1200 to 200 rad/s. The results for both models with the initial parameters from Table III and the refined parameter settings are given in Table I, with a zoomed plot of some of the eigenvalues shown in Fig. 5.

From Table I, it can be clearly seen that the eigenvalues of the two VSM implementations are quite different when the same SM electrical parameters are used. It is also noticed from Fig. 5 and Table I that the DEM model with the initial low value of the stator resistance result in a pair of poorly damped complex conjugate poles, $\lambda_{7,8}$ with imaginary part of ± 312 , corresponding to oscillations of about 50 Hz, as shown in Fig. 4. However, by increasing the virtual stator resistance, the damping of these eigenvalues can be significantly improved. Similarly, it can also be seen from Table I that the eigenvalues $\lambda_{3,4}$ with high oscillation frequency and poor damping for the initial settings of the QSEM-based implementation can be avoided by changing the system parameters.

V. EXPERIMENTAL VALIDATION

To verify the validity of the developed models, and to demonstrate that they are applicable for further numerical analysis of the small-signal dynamics of the two VSM implementations, their operation have been verified by laboratory experiments.

A. Laboratory Setup

An overview of the experimental setup is shown in Fig 6, while the main parameters are listed in Table II. A three-

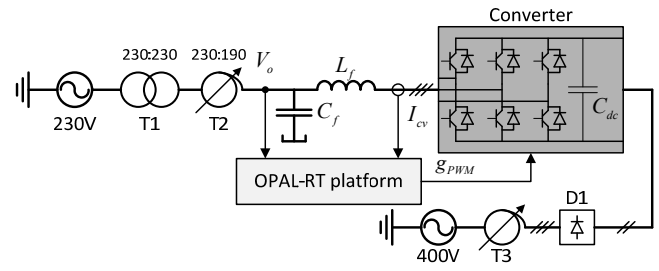


Fig. 6 Configuration of laboratory setup

TABLE II
PARAMETERS LABORATORY TEST

Parameter	Value	Parameter	Value
Rated voltage $V_{S,LL,RMS}$	190 V	Grid resistance, r_g	0.08 pu (1.0 Ω)
Rated power S_b	3 kVA	Filter inductance, L_f	0.05 pu (2.0 mH)
Rated grid frequency f_g	50 Hz	Filter resistance, r_{ff}	0.008 pu (0.1 Ω)
Grid inductance L_g	0.039 pu (1.5mH)	Filter capacitance, C_f	0.19 pu (50 μ F)
Switching frequency, f_{sw}	10 kHz	Sampling frequency, f_{samp}	10 kHz

phase, two-level, IGBT-based VSC was used for the experiments. An LC-filter (L_f and C_f) is connected between the ac terminals of the converter and an adjustable transformer (T2) fed from a 230V ac grid through an isolating transformer (T1). The dc-side of the converter is supplied from a diode rectifier (D1) fed from a separate 400 V grid and an adjustable transformer (T3). The control, monitoring and high-level protection of the converter are implemented in an OPAL-RT platform, which is executing in real-time the Simulink-based control system implementation used to generate the time-domain simulation results in section IV.A.

For the presented experiments, the adjustable transformer T1 is adjusted to give 190V_{RMS} on the filter capacitors when the converter is not in operation. The adjustable transformer T3 is adjusted to provide 300V rectified voltage to the dc-capacitor of the converter.

B. Experimental results with the two VSM implementations

For obtaining the presented results, the voltage and frequency references are set to 1.0 pu. The set-point values for active and reactive power are both initially zero and the converter is allowed to reach steady state before imposing a step from 0 to 0.5 pu in the active power reference. The response in power flow and filter inductor currents is shown in Fig. 7 for both the DEM and QSEM-based VSM implementations.

The laboratory measurements in Fig. 7 are shown together with results from equivalent numerical simulations, labelled with "(mea)" and "(sim)", respectively. The results from the experimental setup verifies that the simulation model is able to replicate the behavior of a practical VSM implementation. However, some small deviations between the experimental results and the simulations can be seen in Fig. 7. These deviations are mainly associated with limited accuracy in the

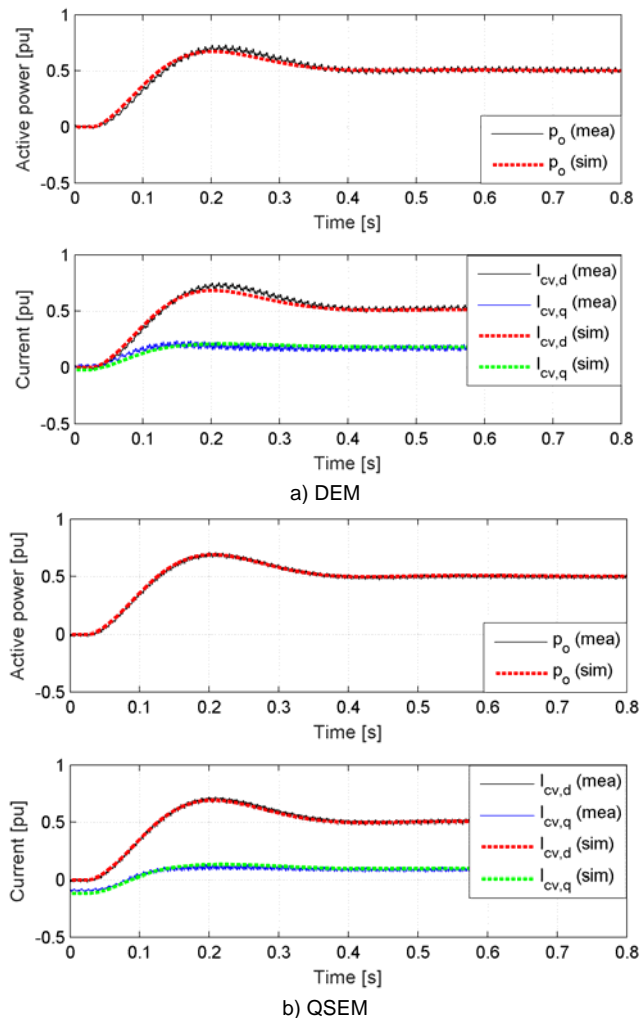


Fig. 7 Comparison between simulation and laboratory measurements for (a) DEM-implementation and (b) QSEM implementation.

parameter for the LC filter and the grid impedance, especially the resistances.

Small differences can be also observed between $I_{cv,q}$ for the DEM and QSEM implementations in fig 7, which are found to be caused by a slight difference in the ac grid voltage ($\sim 2.5V$) when conducting the different experiments. This difference is taken into account in the simulations by adjusting the voltage for the QSEM simulation accordingly.

It can also be noted that the no significant problems with oscillations for the DEM-based implementation were experience in the laboratory setup, and a reasonably damped response was achieved even with very low values of r_s . The main reason for this difference compared to the simulation results in section IV.A is the higher equivalent grid resistance in the laboratory environment than what is reasonable to assume for a high power application (0.08 pu in the experiment compared to 0.005pu in the simulation study). Thus, the grid resistance in the experimental setup provides sufficient damping to prevent instability, even if r_s is reduced to zero. This was also verified by simulations with the parameters from the laboratory setup, which demonstrated that stability could be ensured for all values of r_s down to zero.

A high value of the filter crossover frequency, ω_{cf} , for the QSEM implementation will later in this paper be shown to cause instability. The effect of increasing ω_{cf} was therefore also tested in the laboratory. The system stability was found to be very sensitive to this parameter. The laboratory system is stable for ω_{cf} equal to 1090 rad/s while it becomes very oscillatory for ω_{cf} exceeding 1190 rad/s. For simulations with the set of parameters used in section IV, the system was still stable but close to the stability limit with this value of ω_{cf} . Thus, the behavior matched very well with the numerical simulation concerning the threshold for the transition from stable to unstable conditions. In both cases, a robust performance of the QSEM implementation can be ensured as long as ω_{cf} is kept below about 1000 rad/s.

VI. PARAMETER SENSITIVITY ANALYSIS

This section presents a systematic parametric sensitivity analysis for the two investigated VSM implementations with parameters from Table III. This analysis is presented in order to identify the parameters with the strongest influence on the critical eigenvalues and to reveal how modifying these parameters will influence the system dynamics.

The eigenvalue parametric sensitivities are defined as the partial derivative of the system eigenvalues with respect to a set of predefined system parameters [24]. The real part and the imaginary part of the sensitivities are associated to the derivatives of the pole location along the real and the imaginary axis respectively. The normalized sensitivity $\alpha_{n,k}$ of the parameter ρ_k with respect to the eigenvalue λ_n can be expressed by (22), where Ψ_n^T and Φ_n are the left and right eigenvectors associated to the eigenvalue λ_n .

$$\alpha_{n,k} = \rho_k \frac{\partial \lambda_n}{\partial \rho_k} = \rho_k \frac{\Phi_n^T \frac{\partial \mathbf{A}}{\partial \rho_k} \Psi_n}{\Phi_n^T \Psi_n} \quad (22)$$

In this paper, the parametric sensitivities have also been normalized with a scaling based on the parameter value at the linearization point. This scaling is introduced to improve the readability and the intuitive impression of relative parameter sensitivity for graphical representation.

A. Parametric Sensitivity for the DEM implementation

The real part of the eigenvalue parametric sensitivities for the DEM-based VSM implementation are shown in Fig. 8. The colors indicate the percent change, with blue associated to modes becoming slower for an increase of the parameter. The color scale is limited to the range -1 to 1 and saturated for higher values. The modes 7 and 8 are close to 50Hz oscillations with a rather low relative damping of 0.011. The parametric sensitivities suggest that better damping can be obtained by increasing r_s or r_g and alternatively by decreasing ω_{cf} , k_q , l_s , k_{iv} , k_{pv} or l_g . Indeed, an increase in the virtual stator resistance moves the pole to the left and increases the relative damping with little effect on other modes, as shown in the parametric sweep in Fig. 9 where r_s varies in the range from 0.001 pu (blue) to 0.2 pu (red). Vice versa, a reduction in the stator resistance can shift the poles towards the right side of the complex plane and generate instability for values lower than 0.0047 pu. The effect is also illustrated in the time domain by

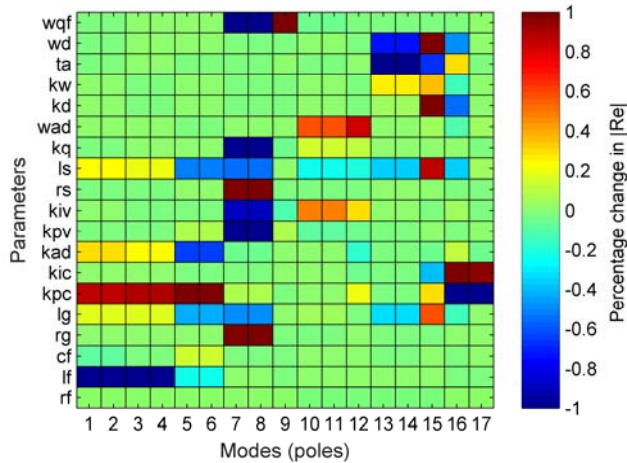


Fig. 8 Parametric sensitivity for the real part of the eigenvalues for DEM-based VSM (percent change in absolute value of real part of each mode for a 1% increase of parameter value) – initial tuning

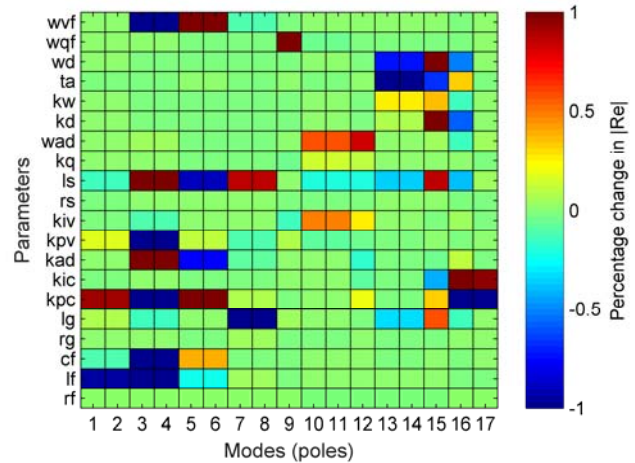


Fig. 11 Parametric sensitivity for the real part of the eigenvalues for QSEM-based VSM implementation (percent change in absolute value of real part of each mode for a 1% increase of parameter value) – initial tuning

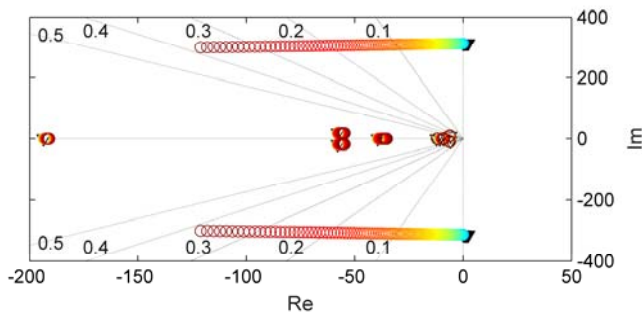


Fig. 9 Eigenvalues of DEM-based model for a parametric sweep of the VSM stator resistance (sweep of r_s from 0.001pu (blue) to 0.2pu (red))

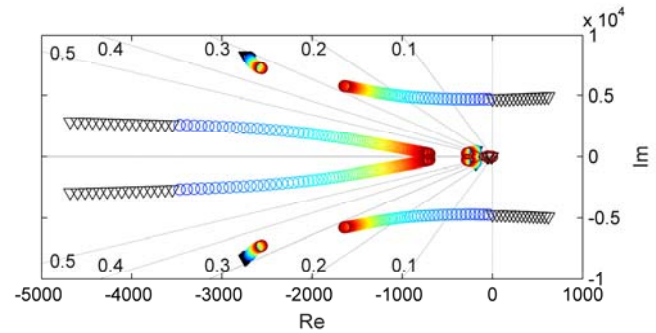


Fig. 12 Eigenvalues of QSEM-based model for a parametric sweep of the voltage filtering crossover frequency (from 2000 (blue) to 200rad/s (red)).

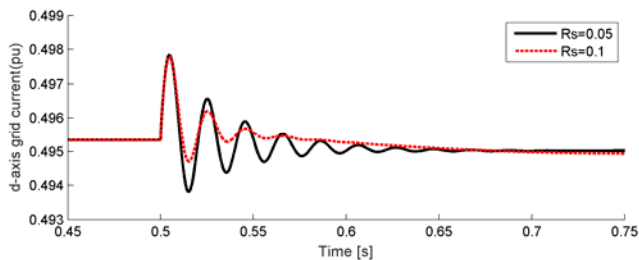


Fig. 10 Effect of r_s on the transient performances of DEM-based VSM implementation with the same disturbance as in Fig. 4

Fig. 10. Thus, the DEM implementation requires a value for the stator resistance that is in general higher than for a real SM. Although, this might still be acceptable for a VSM, since it only implies virtual losses that do not influence the efficiency, it does have implications for the power flow control. A value equal to 0.1 pu is set for the remaining of the paper.

B. Parametric Sensitivity for the QSEM implementation

The eigenvalue parametric sensitivities for the QSEM implementation are shown in Fig. 11 and indicate a strong sensitivity to the bandwidth ω_{vf} (wvf in the figure) of the voltage filtering for the critical eigenvalues 3 and 4. Thus, the eigenvalue trajectory is shown in Fig. 12 for a sweep of ω_{vf} within the range from 50 rad/s (red) to 2000 rad/s (blue). This

plot clearly shows that the QSEM-based VSM implementation can cause instability related to the LC filter oscillations without appropriate filtering of the capacitor voltage measurements used for calculating the VSC current references. However, when appropriate filter settings (i.e. ω_{vf} = 200rad/s, as assumed in the rest of the paper) are selected, the stability problems can be avoided with good margin.

VII. PERFORMANCE DEPENDENCY ON GRID CONDITIONS

The comparative analysis between the two implementations is continued in this section by assessing the impact of the grid characteristics on stability and dynamic performances. For simplicity, the stiffness of the grid is modified by acting only on the grid inductance. The eigenvalue trajectory obtained by sweeping the grid inductance value from 0.4pu (blue) to 0.005 pu (red) are shown in Fig. 13 a) and b) for the for the DEM and QSEM implementations, respectively.

The parametric sweeps indicate that both implementations have eigenvalues with higher oscillation frequency and poorer damping at low grid inductance. This is mainly due to the LC resonances associated with the filter capacitor and the grid inductance. It can be noticed that the QSEM implementation is having one set of complex conjugate eigenvalues with noticeably lower real part than for the DEM implementation.

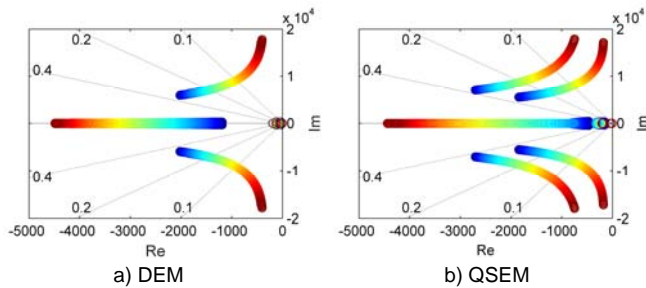


Fig. 13 Eigenvalue trajectory for a parametric sweep of l_g from 0.4 (blue) to 0.005 (red) for the two implementations

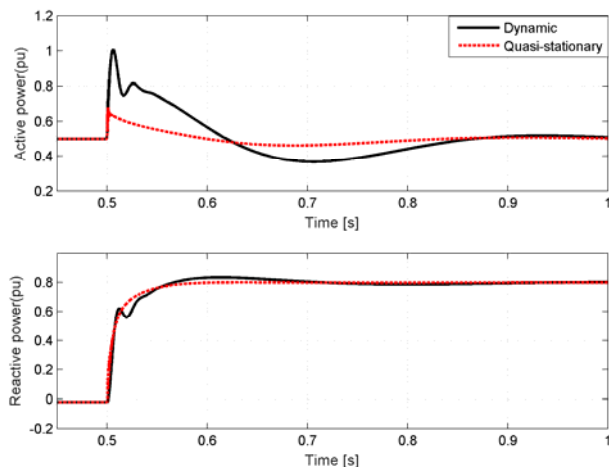


Fig. 14 Comparison of active and reactive power flow after a 10% instant drop in grid voltage (grid d-axis voltage) when operating in a strong grid (grid reactance reduced to 10% of initial value)

This is because the QSEM implementation does not have a dynamic representation of the virtual stator currents like the DEM-based VSM, and instead depend on the measured filter capacitor voltages for calculating the VSC current references. However, as long as sufficient filtering is included in the voltage measurements, a wide stability margin can always be ensured. Furthermore, the poorly damped modes of the QSEM-based VSM are usually not much excited. Thus, satisfactory dynamic characteristics can be obtained for both implementations with a wide range of grid impedances.

Although stability can be ensured for both the DEM and the QSEM implementations, the DEM-based VSMs will rely on the high value of virtual stator resistance. The resulting coupling between active and reactive power flow might be considered disadvantageous, especially in case of strong grid conditions, as shown in Fig. 14. This figure shows how the DEM and QSEM VSMs with the refined parameters from section IV respond to a step in the grid voltage amplitude. Indeed, the upper plot in the figure shows how the DEM implementation implies a significant response in the active power, while the overshoot in the power response for the QSEM is much less noticeable, and the overall response is more damped. Thus, again the QSEM model can be considered to have an advantage since desired dynamic characteristics can be ensured without depending on a high virtual stator resistance.

VIII. CONCLUSION

The eigenvalue analysis and the parameter sensitivity analysis presented in this paper has revealed the main small-signal characteristics of the DEM and QSEM-based VSM implementations. Indeed, the presented analysis has identified the parameters that are critical for system stability, and has shown how both implementations can be tuned to ensure satisfactory small-signal dynamics. However, the DEM-based implementation has the disadvantage that it depends on a high value of the virtual stator resistance to avoid poorly damped synchronous frequency resonance in the SSRF, which is equivalent to poorly damped dc components in the stationary reference frame. Thus, a DEM-based VSM with well-damped response implies a system with significant coupling between active and reactive power control, while this coupling can easily be avoided with the QSEM-based implementation. Even if the DEM-based VSM implementation is more common and studied by a large number of previous publications, the results from the presented analysis demonstrates that the less common QSEM can be a preferable option for VSM implementations with current controlled VSCs.

APPENDIX: SYSTEM PARAMETERS AND STATE EQUATIONS

The system parameters and the default set-points used in this paper are listed in Table III. The non-linear state-space model of the DEM-based VSM implementation are given by the following set of 17 equations:

$$1) \frac{dv_{o,d}}{dt} = \omega_b \omega_{VSM} v_{o,q} + \frac{\omega_b}{c_f} i_{cv,d} - \frac{\omega_b}{c_f} i_{o,d}$$

$$2) \frac{dv_{o,q}}{dt} = -\omega_b \omega_{VSM} v_{o,d} + \frac{\omega_b}{c_f} i_{cv,q} - \frac{\omega_b}{c_f} i_{o,q}$$

TABLE III
PARAMETERS AND SET-POINTS

Parameter	Value	Parameter	Value
Rated voltage $V_{S,LL,RMS}$	690 V	Current controller gain: k_{pc}, k_{ic}	1.27 15
Rated power S_b	2.75 MVA	Voltage feed forward in current controller k_{ffv}	0
Rated angular frequency ω_b	$2\pi \cdot 50$ Hz	Voltage feed forward in voltage controller k_{ffe}	0
Grid volt. $\hat{v}_{g,d}, \hat{v}_{g,q}$	1.0/0.0 pu	Active damping gain k_{AD}	1.5
Grid angular frequency ω_g	1.0 pu	Active damping ω_{AD}	50 rad/s
Grid inductance l_g	0.20 pu	Frequency controller gain k_ω	20
Grid resistance r_g	0.005 pu	Voltage controller gain: k_{pv}, k_{iv}	0.29 92
Filter inductance l_f	0.08 pu	Reactive power filter ω_{qf}	200 rad/s
Filter resistance r_f	0.003 pu	Reactive power droop gain k_q	0.1 pu
Filter capacitance c_f	0.074 pu	Power reference p^*	0.5 pu
Inertia constant T_d	4 s	Reactive power reference q^*	0.0 pu
Damping coefficient k_d	40	Voltage reference v^*	1.0 pu
Damping filter ω_d	5 rad/s	Frequency reference ω_{VSM}^*	1.0 pu
SM inductance l_s	0.25 pu	Voltage low-pass filter for QSEM VSM ω_{vf}	1200* rad/s
SM resistance r_s	0.01** pu		

* 200 rad/s in QSEM implementation after tuning

** 0.1 pu in DEM implementation after tuning

IEEE TRANSACTIONS ON INDUSTRIAL ELECTRONICS

$$\begin{aligned}
 3) \quad \frac{di_{cv,d}}{dt} &= -\frac{\omega_b(1-k_{fv}+k_{ad})}{l_f}v_{o,d} - \frac{\omega_b(k_{pc}+r_f)}{l_f}i_{cv,d} + \frac{\omega_b k_{ic}}{l_f}\gamma_d - \frac{\omega_b k_{ad}}{l_f}\varphi_d + \frac{\omega_b k_{pc}}{l_f}i_{s,d} \\
 4) \quad \frac{di_{cv,q}}{dt} &= -\frac{\omega_b(1-k_{fv}+k_{ad})}{l_f}v_{o,q} - \frac{\omega_b(k_{pc}+r_f)}{l_f}i_{cv,q} + \frac{\omega_b k_{ic}}{l_f}\gamma_q - \frac{\omega_b k_{ad}}{l_f}\varphi_q + \frac{\omega_b k_{pc}}{l_f}i_{s,q} \\
 5) \quad \frac{d\gamma_d}{dt} &= -i_{cv,d} + i_{s,d} & 6) \quad \frac{d\gamma_q}{dt} &= -i_{cv,q} + i_{s,q} \\
 7) \quad \frac{di_{o,d}}{dt} &= \frac{\omega_b}{l_g}v_{o,d} - \frac{\omega_b r_g}{l_g}i_{o,d} + \omega_b \omega_{VSM} i_{o,q} - \frac{\omega_b}{l_g}\tilde{v}_{g,d} \cos(\delta\theta_{VSM}) - \frac{\omega_b}{l_g}\tilde{v}_{g,q} \sin(\delta\theta_{VSM}) \\
 8) \quad \frac{di_{o,q}}{dt} &= \frac{\omega_b}{l_g}v_{o,q} - \frac{\omega_b r_g}{l_g}i_{o,q} - \omega_b \omega_{VSM} i_{o,d} - \frac{\omega_b}{l_g}\tilde{v}_{g,q} \cos(\delta\theta_{VSM}) + \frac{\omega_b}{l_g}\tilde{v}_{g,d} \sin(\delta\theta_{VSM}) \\
 9) \quad \frac{d\varphi_d}{dt} &= -\omega_{ad}v_{o,d} - \omega_{ad}\varphi_d & 10) \quad \frac{d\varphi_q}{dt} &= -\omega_{ad}v_{o,q} - \omega_{ad}\varphi_q \\
 11) \quad \frac{d\xi}{dt} &= -\sqrt{v_{o,d}^2 + v_{o,q}^2} - k_q q_m + k_q \hat{q}^* + \hat{v}^* \\
 12) \quad \frac{di_{s,d}}{dt} &= -\frac{\omega_b}{l_s}v_{o,d} + \frac{\omega_b(k_{fe}-k_{pv})}{l_s}\sqrt{v_{o,d}^2 + v_{o,q}^2} + \frac{\omega_b k_{iv}}{l_s}\xi - \frac{\omega_b r_s}{l_s}i_{s,d} \dots \\
 & \quad + \omega_b \omega_{VSM} i_{s,q} - \frac{\omega_b k_{pv} k_q}{l_s}q_m + \frac{\omega_b k_{pv} k_q}{l_s}\hat{q}^* + \frac{\omega_b k_{pv}}{l_s}\hat{v}^* \\
 13) \quad \frac{di_{s,q}}{dt} &= -\frac{\omega_b}{l_s}v_{o,q} - \frac{\omega_b r_s}{l_s}i_{s,q} - \omega_b \omega_{VSM} i_{s,d} \\
 14) \quad \frac{dq_m}{dt} &= -i_{o,q}v_{o,d}\omega_{gf} + i_{o,d}v_{o,q}\omega_{gf} - q_m\omega_{gf} \\
 15) \quad \frac{d\omega_{VSM}}{dt} &= -\frac{1}{T_a}i_{o,d}v_{o,d} - \frac{1}{T_a}i_{o,q}v_{o,q} - \frac{(k_d+k_w)}{T_a}\omega_{VSM} + \frac{k_d}{T_a}\kappa + \frac{1}{T_a}p^* + \frac{k_w}{T_a}\omega_{VSM}^* \\
 16) \quad \frac{d\delta\theta_{VSM}}{dt} &= \omega_b \omega_{VSM} - \omega_b \omega_g \\
 17) \quad \frac{d\kappa}{dt} &= \omega_a \omega_{VSM} - \kappa \omega_d
 \end{aligned}$$

The state equations of the QSEM model that differ from the DEM model are listed in the following:

$$\begin{aligned}
 3) \quad \frac{di_{cv,d}}{dt} &= -\frac{\omega_b(1-k_{fv}+k_{ad})}{l_f}v_{o,d} + \frac{\omega_b k_{pc} r_s (k_{fe} - k_{pv})}{l_f (r_s^2 + \omega_{VSM}^2 l_s^2)} \sqrt{v_{o,d}^2 + v_{o,q}^2} \\
 & \quad - \frac{\omega_b(k_{pc}+r_f)}{l_f}i_{cv,d} + \frac{\omega_b k_{ic}}{l_f}\gamma_d - \frac{\omega_b k_{ad}}{l_f}\varphi_d + \frac{\omega_b k_{pc} k_{iv} r_s}{l_f (r_s^2 + \omega_{VSM}^2 l_s^2)} \xi \\
 & \quad - \frac{\omega_b k_{pc} r_s}{l_f (r_s^2 + \omega_{VSM}^2 l_s^2)} v_{m,d} - \frac{\omega_b k_{pc} l_s}{l_f (r_s^2 + \omega_{VSM}^2 l_s^2)} \omega_{VSM} v_{m,q} \\
 & \quad - \frac{\omega_b k_{pc} k_{pv} k_q r_s}{l_f (r_s^2 + \omega_{VSM}^2 l_s^2)} q_m + \frac{\omega_b k_{pc} k_{pv} k_q r_s}{l_f (r_s^2 + \omega_{VSM}^2 l_s^2)} \hat{q}^* + \frac{\omega_b k_{pc} k_{pv} r_s}{l_f (r_s^2 + \omega_{VSM}^2 l_s^2)} \hat{v}^* \\
 4) \quad \frac{di_{cv,q}}{dt} &= -\frac{\omega_b(1-k_{fv}+k_{ad})}{l_f}v_{o,q} - \frac{\omega_b k_{pc} l_s (k_{fe} - k_{pv})}{l_f (r_s^2 + \omega_{VSM}^2 l_s^2)} \omega_{VSM} \sqrt{v_{o,d}^2 + v_{o,q}^2} \\
 & \quad - \frac{\omega_b(k_{pc}+r_f)}{l_f}i_{cv,q} + \frac{\omega_b k_{ic}}{l_f}\gamma_q - \frac{\omega_b k_{ad}}{l_f}\varphi_q - \frac{\omega_b k_{pc} k_{iv} l_s}{l_f (r_s^2 + \omega_{VSM}^2 l_s^2)} \omega_{VSM} \xi \\
 & \quad + \frac{\omega_b k_{pc} l_s}{l_f (r_s^2 + \omega_{VSM}^2 l_s^2)} \omega_{VSM} v_{m,d} - \frac{\omega_b k_{pc} r_s}{l_f (r_s^2 + \omega_{VSM}^2 l_s^2)} v_{m,q} + \frac{\omega_b k_{pc} k_{pv} k_q l_s}{l_f (r_s^2 + \omega_{VSM}^2 l_s^2)} \omega_{VSM} q_m \\
 & \quad - \frac{\omega_b k_{pc} k_{pv} k_q l_s}{l_f (r_s^2 + \omega_{VSM}^2 l_s^2)} \omega_{VSM} \hat{q}^* - \frac{\omega_b k_{pc} k_{pv} l_s}{l_f (r_s^2 + \omega_{VSM}^2 l_s^2)} \omega_{VSM} \hat{v}^* \\
 5) \quad \frac{d\gamma_d}{dt} &= -i_{cv,d} + \frac{r_s(k_{fe}-k_{pv})}{r_s^2 + \omega_{VSM}^2 l_s^2} \sqrt{v_{o,d}^2 + v_{o,q}^2} + \frac{k_{iv} r_s}{r_s^2 + \omega_{VSM}^2 l_s^2} \xi - \frac{r_s}{r_s^2 + \omega_{VSM}^2 l_s^2} v_{m,d} \\
 & \quad - \frac{l_s}{r_s^2 + \omega_{VSM}^2 l_s^2} \omega_{VSM} v_{m,q} - \frac{k_{pv} k_q r_s}{r_s^2 + \omega_{VSM}^2 l_s^2} q_m + \frac{k_{pv} k_q r_s}{r_s^2 + \omega_{VSM}^2 l_s^2} \hat{q}^* + \frac{k_{pv} r_s}{r_s^2 + \omega_{VSM}^2 l_s^2} \hat{v}^* \\
 6) \quad \frac{d\gamma_q}{dt} &= -i_{cv,q} - \frac{l_s(k_{fe}-k_{pv})}{r_s^2 + \omega_{VSM}^2 l_s^2} \omega_{VSM} \sqrt{v_{o,d}^2 + v_{o,q}^2} - \frac{k_{iv} l_s}{r_s^2 + \omega_{VSM}^2 l_s^2} \omega_{VSM} \xi \\
 & \quad + \frac{l_s}{r_s^2 + \omega_{VSM}^2 l_s^2} \omega_{VSM} v_{m,d} - \frac{r_s}{r_s^2 + \omega_{VSM}^2 l_s^2} v_{m,q} + \frac{k_{pv} k_q l_s}{r_s^2 + \omega_{VSM}^2 l_s^2} \omega_{VSM} q_m \\
 & \quad - \frac{k_{pv} k_q l_s}{r_s^2 + \omega_{VSM}^2 l_s^2} \omega_{VSM} \hat{q}^* - \frac{k_{pv} l_s}{r_s^2 + \omega_{VSM}^2 l_s^2} \omega_{VSM} \hat{v}^*
 \end{aligned}$$

$$12) \quad \frac{dv_{m,d}}{dt} = \omega_{gf} v_{o,d} - \omega_{gf} v_{m,d} \qquad 13) \quad \frac{dv_{m,q}}{dt} = \omega_{gf} v_{o,q} - \omega_{gf} v_{m,q}$$

REFERENCES

- [1] H.-P. Beck, R. Hesse, "Virtual Synchronous Machine," in *Proc. of the 9th Int. Conf. on Electrical Power Quality and Utilisation*, Barcelona, Spain, 9-11 Oct. 2007, 6 pp.
- [2] J. Driesen, K. Visscher, "Virtual Synchronous Generators," in *Proc. of the IEEE PES 2008 General Meeting: Conversion and Delivery of Energy in the 21st Century*, Pittsburgh, Pennsylvania, USA, 20-24 Jul. 2008, 3 pp.
- [3] K. Visscher, S. W. H. De Haan, "Virtual Synchronous Machines (VSG's) for Frequency Stabilization in Future Grids with a Significant Share of Decentralized Generation," in *Proc. of the CIRED seminar 2008: SmartGrids for Distribution*, Frankfurt, Germany, 23-24 Jun. 2008, 4 pp.
- [4] R. Hesse, D. Turschner, H.-P. Beck, "Micro grid stabilization using the Virtual Synchronous Machine (VISMA)," in *Proc. of the Int. Conf. on Renewable Energies and Power Quality, ICREPQ'09*, Valencia, Spain, 15-17 Apr. 2009, 6 pp.
- [5] Y. Chen, R. Hesse, D. Turschner, H.-P. Beck, "Investigation of the Virtual Synchronous Machine in the Island Mode," in *Proc. of the 2012 3rd IEEE Innovative Smart Grid Technologies Europe Conf., ISGT Europe 2012*, Berlin, Germany, 15-17 Oct. 2012, 6 pp.
- [6] S. D'Arco, J. A. Suul, "Virtual Synchronous Machines – Classification of Implementations and Analysis of Equivalence to Droop Controllers for Microgrids," in *Proc. of IEEE PowerTech Grenoble 2013*, Grenoble, France, 16-20 Jun. 2013, 7 pp.
- [7] Y. Chen, R. Hesse, D. Turschner, H.-P. Beck, "Improving the Grid Power Quality Using Virtual Synchronous Machines," in *Proc. of the 2011 Int. Conf. on Power Engineering, Energy and Electrical Drives, POWERENG 2011*, Torremolinos, Spain, 11-13 May 2011, 6 pp.
- [8] Y. Chen, R. Hesse, D. Turschner, H.-P. Beck, "Dynamic Properties of the Virtual Synchronous Machine (VSIMA)" in *Proc. of the Int. Conf. on Renewable Energies and Power Quality, ICREPQ'11*, Las Palmas, Spain, 13-15 Apr. 2011, 5 pp.
- [9] P. Rodriguez, I. Candela, A. Luna, "Control of PV Generation Systems using the Synchronous Power Controller," in *Proc. of the 2013 IEEE Energy Conversion Congress and Expo., ECCE 2013*, Denver, Colorado, USA, 15-19 Sept. 2013, pp. 993-998
- [10] C. Li, R. Burgos, I. Cvetkovic, D. Boroyevich, L. Mili, P. Rodriguez, "Analysis and Design of Virtual Synchronous Machine Based STATCOM Controller," in *Proc. of the 2014 15th Workshop on Control and Modeling for Power Electronics, COMPEL 2014*, Santander, Spain, 22-25 Jun. 2014, 6 pp.
- [11] X. Wang, M. Yue, E. Muljadi, "PV Generation Enhancement with a Virtual Inertia Emulator to Provide Inertial Response to the Grid," in *Proc. of the 2014 IEEE Energy Conversion Congress and Expo., ECCE 2014*, Pittsburgh, Pennsylvania, USA, 14-18 Sept. 2014, pp. 17-23
- [12] Y. Chen, R. Hesse, D. Turschner, H.-P. Beck, "Comparison of methods for implementing virtual synchronous machine on inverters," in *Proc. of the Int. Conf. on Renewable Energies and Power Quality, ICREPQ'12*, Santiago de Compostela, Spain, 28-30 Mar. 2012, 6 pp.
- [13] Q.-C. Zhong, G. Weiss, "Synchronverters: Inverters That Mimic Synchronous Generators," *IEEE Trans. on Ind. Electron.*, vol. 58, no. 4, pp. 1259-1267, Apr. 2011
- [14] Q.-Z. Chong, P.-L. Nguyen, Z. Ma, W. Sheng, "Self-Synchronized Synchronverters: Inverters Without a Dedicated Synchronization Unit," in *IEEE Trans. on Power Electron.*, Vol. 29, No. 2, pp. 617-630, Feb. 2014
- [15] K. Sakimoto, Y. Miura, T. Ise, "Stabilization of a power system with a distributed generator by a virtual synchronous generator function," in *Proc. of the 8th Int. Conf. on Power Electron. – ECCE Asia*, Jeju, Korea, 30 May- 3 Jun. 2011, 8 pp.
- [16] T. Shintai, Y. Miura, T. Ise, "Oscillation Damping of a Distributed Generator Using a Virtual Synchronous Generator," in *IEEE Trans. on Power Deliv.*, Vol. 29, No. 2, pp 668-676, Apr. 2014
- [17] H. Wu, X. Ruan, D. Yang, X. Chen, W. Zhao, Z. Lv, Q.-C. Zhong, "Small-Signal Modeling and Parameters Design for Virtual Synchronous Generators," in *IEEE Trans. on Ind. Electron.*, Vol. 63, No. 7, pp. 4292-4303, Jul. 2016

- [18] S. D'Arco; J. A. Suul; O. B. Fosso, "Control System Tuning and Stability Analysis of Virtual Synchronous Machines," in *Proc. of the 2013 IEEE Energy Conversion Congress and Expo., ECCE 2013*, Denver, Colorado, USA, 15-19 Sept. 2013, pp. 2664-2671
- [19] S. D'Arco, J. A. Suul, O. B. Fosso, "Small-Signal Modelling and Parametric Sensitivity of a Virtual Synchronous Machine," in *Proc. of the 18th Power Systems Computation Conf., PSCC 2014*, Wroclaw, Poland, 18-22 August 2014, 9 pp.
- [20] S. D'Arco, J. A. Suul, O. B. Fosso, "A Virtual Synchronous Machine Implementation for Distributed Control of Power Converters in SmartGrids," in *Electric Power System Research*, Vol. 122, pp. 180-197, May 2015
- [21] M. Ashabani, Y. A.-R. I. Mohamed, "Integrating VSCs to Weak Grids by Nonlinear Power Damping Controller With Self-Synchronization Capability," in *IEEE Trans. on Power Syst.*, Vol. 29, No. 2, pp. 805-8014, Mar. 2014
- [22] Y. Hirase, K. Abe, K. Sugimoto, Y. Shindo, "A Grid-Connected Inverter with Virtual Synchronous Generator Model of Algebraic Type," in *Electrical Engineering in Japan*, vol. 184, no. 4, 2013, pp. 10-21, translated from *IEEJ Trans. on Power and Energy*, vol. 132, no. 4, pp. 371-380, Apr. 2012
- [23] K.-I. Sakimoto, K. Sagimoto, Y. Shindo, "Low Voltage Ride Through Capability of a Grid Connected Inverter based on the Virtual Synchronous Generator," in *Proc. of the IEEE 10th International Conf. on Power Electron. and Drive Syst.*, PEDS 2013, Kitakyushu, Japan, 22-25 April 2013, pp. 1066-1071
- [24] P. Kundur, "Power System Stability and Control," McGraw-Hill, New York, 1994
- [25] N. Kroutikova, C. A. Hernandez-Aramburo, T. C. Green, "State-space model of grid-connected inverters under current control mode," in *IET Electr. Power. Appl.*, Vol. 1, No. 3, pp. 329-338, May 2007
- [26] O. Mo, M. Hernes, K. Ljøkelsoy, "Active Damping of Oscillations in LC-filter for Line Connected, Current Controlled, PWM Voltage Source Converters," in *Proc. of the 10th European Conf. on Power Electronics and Appl.*, EPE 2003, Toulouse, France, 2-4 Sept. 2003, 10 pp.
- [27] M. Malinowski, M. P. Kazmierkowski, S. Bernet, "New Simple Active Damping of Resonance in Three-Phase PWM Converter with LCL Filter," in *Proc. of the 2005 IEEE Int. Conf. on Ind. Technol., ICIT 2005*, Hong Kong, 14-17 December 2005, pp. 861-865
- [28] J. Machowski, J. W. Bialek, J. R. Bumby, "Power System Dynamics and Stability," Chichester, UK, Wiley, 1997, Chapter 5
- [29] J. A. Suul, S. D'Arco, G. Guidi, "Virtual Synchronous Machine-based Control of a Single-phase Bi-directional Battery Charger for Providing Vehicle-to-Grid Services," in *Proc. of the 9th Int. Conf. on Power Electron. - ICPE 2015-ECCE Asia*, Seoul, Korea, 1-5 Jun. 2015, pp. 742-749
- [30] W. Leonhard, "Control of Electrical Drives," Springer Verlag, Heidelberg, 1985
- [31] C. Bajracharya, M. Molinas, J. A. Suul, T. M. Undeland, "Understanding of tuning techniques of converter controllers for HVDC," in *Proc. of the Nordic Workshop on Power and Ind. Electron., NORPIE 2008*, 9-11 June 2008, Helsinki, Finland, 8. pp.
- [32] A. E. Fitzgerald, C. Kingsley Jr., S. D. Umans, "Electric Machinery," 6th ed., McGraw Hill, New York, NY, USA, 2003
- [33] J. Wang, Y. Wang, Y. Gu, W. Li, X. He, "Synchronous Frequency Resonance of Virtual Synchronous Generators and Damping Control," in *Proc. of the 9th Int. Conf. on Power Electron.*, ICPE-ECCE Asia, Seoul, Korea, 1-5 June 2015, pp. 1011-1016



Olve Mo was born in Norway in 1965. He received the M.Sc. degree and the Dr.Ing. degree in Electrical Engineering from the Norwegian Institute of Technology (NTH) in Trondheim, Norway, in 1988 and 1993, respectively.

Since 2014, he has been working at SINTEF Energy Research where he is currently Research Scientist. His former experience include eight years at Marine Cybernetics, developing simulator based testing technology for control systems software on advanced offshore vessels, five years former employment at SINTEF Energy Research, five years at Siemens in Trondheim working with switchgear deliveries to the oil and gas industry, and two years as associate professor at the High Voltage Section at NTNU. His current research interests are related to power converters and energy storage in power systems, including wind farms and marine propulsion systems.



Salvatore D'Arco received the M.Sc. and Ph.D. degrees in electrical engineering from the University of Naples "Federico II," Naples, Italy, in 2002 and 2005, respectively.

From 2006 to 2007, he was a postdoctoral researcher at the University of South Carolina, Columbia, SC, USA. In 2008, he joined ASML, Veldhoven, the Netherlands, as a Power Electronics Designer, where he worked until 2010. From 2010 to 2012, he was a postdoctoral researcher in the Department of Electric Power Engineering at the Norwegian University of Science and Technology (NTNU), Trondheim, Norway. In 2012, he joined SINTEF Energy Research where he currently works as a Research Scientist. He is the author of more than 50 scientific papers and is the holder of one patent. His main research activities are related to control and analysis of power-electronic conversion systems for power system applications, including real-time simulation and rapid prototyping of converter control systems.



Jon Are Suul (M'11) received the M.Sc. and PhD degrees from the Department of Electric Power Engineering at the Norwegian University of Science and Technology (NTNU), Trondheim, Norway, in 2006 and 2012, respectively.

From 2006 to 2007, he was with SINTEF Energy Research, Trondheim, where he was working with simulation of power electronic converters and marine propulsion systems until starting his PhD studies. Since 2012, he has resumed a part-time position as a Research Scientist at SINTEF Energy Research while also working as a part-time postdoctoral researcher at the Department of Electric Power Engineering of NTNU. His research interests are mainly related to analysis and control of power electronic converters in power systems and for renewable energy applications.